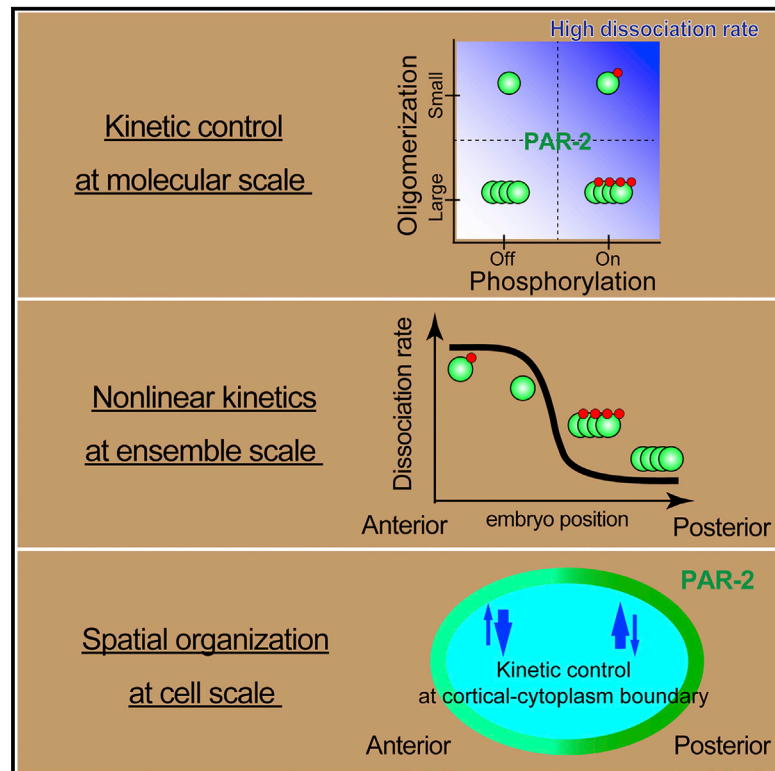# Cortical Polarity of the RING Protein PAR-2 Is Maintained by Exchange Rate Kinetics at the Cortical-Cytoplasmic Boundary

Graphical Abstract

Authors

Yukinobu Arata, Michio Hiroshima, Chan-Gi Pack, ..., Hugo B. Brandão, Tatsuo Shibata, Yasushi Sako

Correspondence

arata@riken.jp (Y.A.), sako@riken.jp (Y.S.)

In Brief

Through mathematical modeling and in-vivo measurements of PAR-2 polarity protein dynamics, Arata et al. develop an integrated view of how spatial organization at a cellular scale emerges from protein modifications at a single-molecule scale.

Highlights

- Phosphorylation and oligomerization alter the dynamics of single PAR2 particles in vivo

- Non-linear dynamics are achieved through these different PAR-2 species

- Cortical PAR-2 polarity is reproduced in silico using parameters measured in vivo

- Cortical-cytoplasmic exchange kinetics are critical for PAR-2 polarity

Cell Reports

Article

Cortical Polarity of the RING Protein PAR-2 Is Maintained by Exchange Rate Kinetics at the Cortical-Cytoplasmic Boundary

Yukinobu Arata,[1,12,*] Michio Hiroshima,[1,2] Chan-Gi Pack,[1,3] Ravikrishna Ramanujam,[4] Fumio Motegi,[4] Kenichi Nakazato,[5] Yuki Shindo,[1] Paul W. Wiseman,[6,7] Hitoshi Sawa,[8] Tetsuya J. Kobayashi,[9] Hugo B. Brandão,[6,10] Tatsuo Shibata,[11] and Yasushi Sako[1,*]

[1]Cellular Informatics Laboratory, RIKEN, Wako, Saitama 351-0198, Japan
[2]Laboratory for Cell Signaling Dynamics, Quantitative Biology Center (QBiC), RIKEN, Suita, Osaka 565-0874, Japan
[3]Asan Institute for Life Sciences, University of Ulsan, College of Medicine, Asan Medical Center, Seoul 138-736, Republic of Korea
[4]Temasek Life Sciences Laboratory, Mechanobiology Institute, Department of Biological Sciences, National University of Singapore, Singapore 117604, Singapore
[5]Theoretical Biology Laboratory, RIKEN, Wako, Saitama 351-0198, Japan
[6]Department of Physics, McGill University, Montréal, QC H3A 2T8, Canada
[7]Department of Chemistry, McGill University, Montréal, QC H3A 0B8, Canada
[8]Multicellular Organization Laboratory, National Institute of Genetics, Mishima 411-8540, Japan
[9]Institute of Industrial Science, University of Tokyo, Tokyo 153-8505, Japan
[10]Graduate Program in Biophysics, Harvard University, Boston, MA 02115, USA
[11]Laboratory for Physical Biology, RIKEN Center for Developmental Biology (CDB), Chuo-ku Kobe, Hyogo 650-0047, Japan
[12]Lead Contact
*Correspondence: arata@riken.jp (Y.A.), sako@riken.jp (Y.S.)
http://dx.doi.org/10.1016/j.celrep.2016.07.047

SUMMARY

Cell polarity arises through the spatial segregation of polarity regulators. PAR proteins are polarity regulators that localize asymmetrically to two opposing cortical domains. However, it is unclear how the spatially segregated PAR proteins interact to maintain their mutually exclusive partitioning. Here, single-molecule detection analysis in *Caenorhabditis elegans* embryos reveals that cortical PAR-2 diffuses only short distances, and, as a result, most PAR-2 molecules associate and dissociate from the cortex without crossing into the opposing domain. Our results show that cortical PAR-2 asymmetry is maintained by the local exchange reactions that occur at the cortical-cytoplasmic boundary. Additionally, we demonstrate that local exchange reactions are sufficient to maintain cortical asymmetry in a parameter-free mathematical model. These findings suggest that anterior and posterior PAR proteins primarily interact through the cytoplasmic pool and not via cortical diffusion.

INTRODUCTION

Cell polarity is a mechanism for generating asymmetry in cells and animal embryos. Polarized cells are partitioned into two structurally and physiologically distinct regions, enabling such cells to migrate directionally, change their shape, and divide asymmetrically. This functional partitioning of cells depends on asymmetric cortical localization of polarity proteins (Suzuki and Ohno, 2006; Goldstein and Macara, 2007; Hoege and Hyman, 2013). Localization of polarity proteins is maintained by their recycling rather than by static binding at the cortex (Weiner, 2002; Mayer et al., 2005; Marco et al., 2007). This recycling is regulated by spatially controlled energy-dissipative chemical reactions. The regulatory reactions include phosphorylation of PAR-1, PAR-2, and PAR-3 in *C. elegans* (Hao et al., 2006; Motegi et al., 2011), lethal giant larvae (LGL) and numb in *Drosophila* (Smith et al., 2007; Tian and Deng, 2008), and Pom1p in fission yeast (Hachet et al., 2011). Other reactions include GTP-GDP exchange by Cdc42 GTPase in budding yeast (Marco et al., 2007; Kozubowski et al., 2008) and inositol lipid modification by cortical phosphoinositide 3-kinase (PI3K) in neutrophils (Swaney et al., 2010). It has been suggested that these molecular modifications regulate intracellular dynamics of polarity proteins; however, it is unclear how such modifications drive the asymmetric cortical localization of polarity proteins in vivo.

The PAR proteins are evolutionarily conserved regulators of cell polarity (Suzuki and Ohno, 2006; Goldstein and Macara, 2007; Hoege and Hyman, 2013). PAR-3 (a multi-PDZ domain protein), PAR-6 (a single PDZ domain protein), and atypical protein kinase C (PKC-3/aPKC) all localize asymmetrically on the anterior cortex, whereas PAR-1, PAR-2 (a RING protein), and LGL-1 localize on the posterior cortex. This reciprocal localization is maintained by a mutual exclusion mechanism involving phosphorylation of posteriorly localizing PAR-1, PAR-2, and LGL-1 by PKC-3 (which itself accumulates at the anterior), and phosphorylation of anteriorly localizing PAR-3 by PAR-1 kinase (which, in turn, accumulates at the posterior). This

phosphorylation promotes dissociation of substrate PAR proteins from the cortex (Hao et al., 2006; Hoege et al., 2010; Motegi et al., 2011; Beatty et al., 2013). A previous study using fluorescence recovery after photobleaching (FRAP) showed that the asymmetric localization of PAR-2 and PAR-6 does not involve diffusion barriers, lateral sorting, or active transport on the cortex, and that PAR-2 and PAR-6 diffuse freely across the anterior-posterior (a-p) polarity boundary (Goehring et al., 2011a). These observations led to the polarity-boundary mutual exclusion model, which states that the asymmetric localization of PAR proteins is maintained by dissociating cortical PAR proteins that invade the opposite cortical side via diffusion. However, to date this model has not been tested by comprehensive measurements of PAR protein dynamics in vivo.

In the present study, we used single-molecule detection (SMD) technologies to measure the protein dynamics of PAR-2, which mediates the recruitment of PAR-1 and LGL-1 to the posterior cortex in *C. elegans* embryos (Boyd et al., 1996; Hoege et al., 2010). For SMD, we used an N-terminal GFP fusion PAR-2 protein, which rescues *par-2* mutants. The fusion protein shows spatiotemporal dynamics indistinguishable from those detected by immunostaining of endogenous PAR-2 (Boyd et al., 1996; Cuenca et al., 2003; Hao et al., 2006; Goehring et al., 2011b). Our combined experimental and theoretical work suggests that cortical PAR-2 asymmetry is largely the result of regulatory interactions at the boundary between the cortex and cytoplasm, rather than at the boundary between the cortical polarity domains. This finding is consistent with a model where anterior and posterior PAR proteins interact through the cytoplasm pool and not through cortical diffusion.

RESULTS

Cortical PAR-2 Diffusion Measured by Single-Molecule Imaging in Living *C. elegans* Embryos

To characterize the in-vivo dynamics of PAR-2, we performed single-molecule imaging (SMI) using a fluorescence microscope with a low-angle oblique illumination close to total internal reflection illumination (semi-TIRFM) (Sako, 2006); we visualized GFP::PAR-2 particles on the *C. elegans* embryo cortex far from the surface of the cover glass at a distance greater than the thickness of the eggshell. We found that fluorescent particle distributions observed by semi-TIRFM were similar to fluorescence intensity (FI) distributions observed by confocal microscopy (Figure 1A). The density of fluorescent GFP::PAR-2 particles expressed in wild-type (WT) embryos (GFP::PAR-2) was asymmetric along the a-p axis of the cortex (Figure 1B; Movie S1). The asymmetric distribution was abolished on the cortex of *pkc-3* RNAi embryos (GFP::PAR-2/*pkc-3*(–)), which resulted in a uniform particle distribution (Movie S2), whereas the asymmetry was weakened in WT embryos expressing mutant PAR-2 with phospho-mimic glutamate substitutions at the seven putative PKC-3 sites (Hao et al., 2006) (GFP::pmPAR-2) (Movie S3).

To characterize cortical movements of PAR-2, we performed single-particle tracking. Trajectories of fluorescent PAR-2 particles revealed no directional bias in movement along the a-p axis, but the trajectories were longer on the posterior side of

the cortex due to changes in cortical residence time (Figure 1C). Despite the residence time difference, there was no difference in diffusion coefficient between the anterior and posterior cortical regions in GFP::PAR-2 or between GFP::PAR-2/*pkc-3*(–) and GFP::pmPAR-2 (Figure 1D) as assessed by mean squared displacement (MSD) analysis. The linearity of the MSD curve indicated that cortical PAR-2 movement is well described by a simple diffusion model, with diffusion coefficient (0.05 μm^2/s); this value is comparable to that measured by FRAP in WT embryos (0.09 μm^2/s) (Goehring et al., 2011a).

Oligomer-Size Distribution of Cortical PAR-2 Is Asymmetric along the A-P Axis

Cortical GFP::PAR-2 particles exhibited differing FIs (Figure 1B, insets), raising the possibility that PAR-2 forms oligomers. To test this possibility, we analyzed FI histograms (Figure 2A) and observed that PAR-2 exhibited multiple intensity peaks, whereas the GFP-fused pleckstrin homology (PH) domain derived from mammalian phospholipase C δ1 (PLCδ1) (GFP::PH) (Audhya et al., 2005) exhibited a single or double peak (Figure S1A). The lowest intensity peak of GFP::PH corresponded to the lowest peak of GFP::PAR-2 (Figure 2A), suggesting that these were singly labeled particles. To confirm this, we observed that most fluorescent particles of cortical GFP::PH that mapped to the lowest intensity peak emitted a constant fluorescence signal and were bleached in a single step. Likewise, step sizes of GFP::PAR-2 particles during photobleaching were nearly constant and similar to those of the GFP::PH particles (Figure 2B). Thus, we conclude that the lowest intensity peak of GFP::PAR-2 in the FI histogram represents single molecules and the higher peaks correspond to PAR-2 oligomers.

To study the mechanism of PAR-2 oligomerization, we performed an in vitro binding assay. Glutathione S-transferase (GST)-tagged and GFP-tagged PAR-2 specifically bound untagged PAR-2 in pull-down assays in vitro and in vivo, respectively (Figures 2C and 2D), indicating that PAR-2 can directly bind another PAR-2 protein. However, GFP is known to form a dimer at high concentrations (Zacharias et al., 2002). To confirm whether oligomerization was due to PAR-2 and not GFP, we tested a monomeric mutant GFP fused with PAR-2 (mGFP::PAR-2). The mGFP::PAR-2 still formed larger oligomers having the same maximum size as GFP::PAR-2 (Figures S1D–S1F). We also tested the effect of GFP for protein oligomerization in *C. elegans* using PAR-3 as a control. We found that PAR-3::GFP formed oligomers but a mutant PAR-3::GFP did not; this mutant lacked the conserved region 1 (CR1) domain (Figure 2A), which is responsible for PAR-3 oligomerization in vivo (Benton and St Johnston, 2003a; Mizuno et al., 2003; Li et al., 2010). Together, these results suggest that PAR-2 forms oligomers in vivo by direct homobinding, and not through GFP.

Next, we studied the maximum size of the oligomers. Although the proportion of larger oligomers is underestimated due to non-fluorescent or endogenous PAR-2, we observed that the FI distribution showed a steep decline at the higher intensity tail (Figures S1C and S1D), which is a clear indication of a maximum limit to oligomer size. We estimated the maximum size of PAR-2 oligomers to be tetrameric (Figures S1D–S1F). Interestingly, the
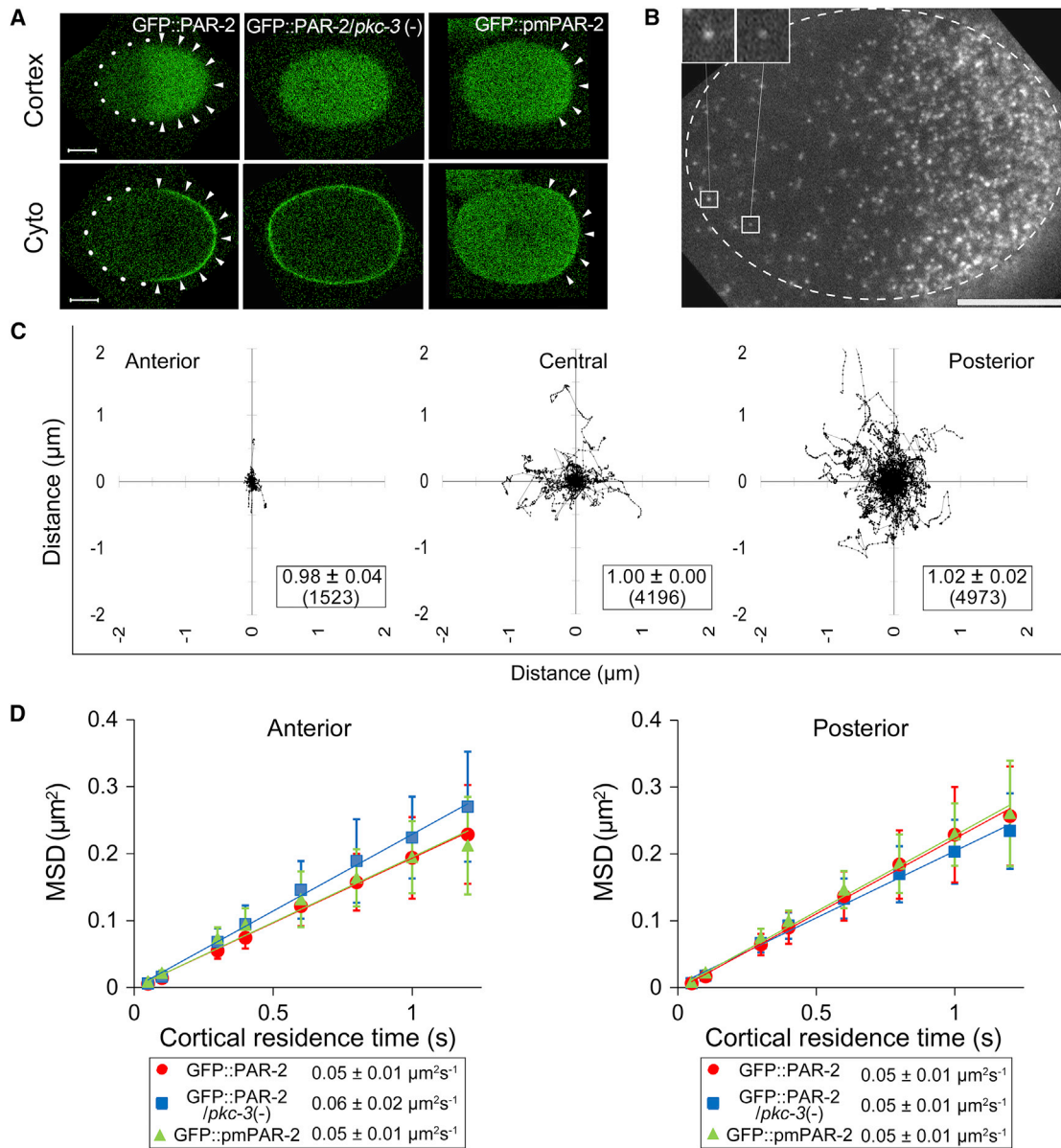
Figure 1. Diffusion of PAR-2 on the Cortex

(A) Representative confocal images for the cortex and cytoplasm. Arrowheads and dots: cortical regions with higher and lower densities of PAR-2, respectively. In all images, the left-hand side indicates the anterior embryo.

(B) Semi-TIRFM images of fluorescent GFP::PAR-2 particles on the embryo cortex. White dashed circle: embryo periphery. Inset: individual particles exhibit different FIs. Particle tracking was performed at a lower density, as shown in Movies S1, S2, and S3.

(C) Representative trajectories of GFP::PAR-2 particles. Origin was set as the position where the particle appeared on the cortex. Inset: mean ratio ± SEM of particles that disappeared from the anterior side compared to the posterior side among four embryos. The number of analyzed particles is indicated in parentheses.

(D) MSD of particle movements as a function of the cortical residence time, were determined from seven, eight, and nine embryos, respectively. Mean values are shown with SEM. The diffusion coefficient (D) was determined by fitting MSD = $4Dt + b$.

Scale bar, 10 μm

size distribution of PAR-2 particles varied along the a-p axis, with smaller particles being enriched at the anterior and larger particles at the posterior cortical regions, respectively (Figures 2E and 2F). This cortical oligomer-size asymmetry was confirmed by fluorescence correlation spectroscopy (FCS) measurements of GFP::PAR-2 and mCherry-fused PAR-2 (Figures S3F and S3G). Moreover, the oligomer-size asymmetry was abolished in GFP::PAR-2/pkc-3(–) and weakened in GFP::pmPAR-2 (Figures S1G and S1H), indicating that phosphorylation by PKC-3 is required for the oligomer-size asymmetry.
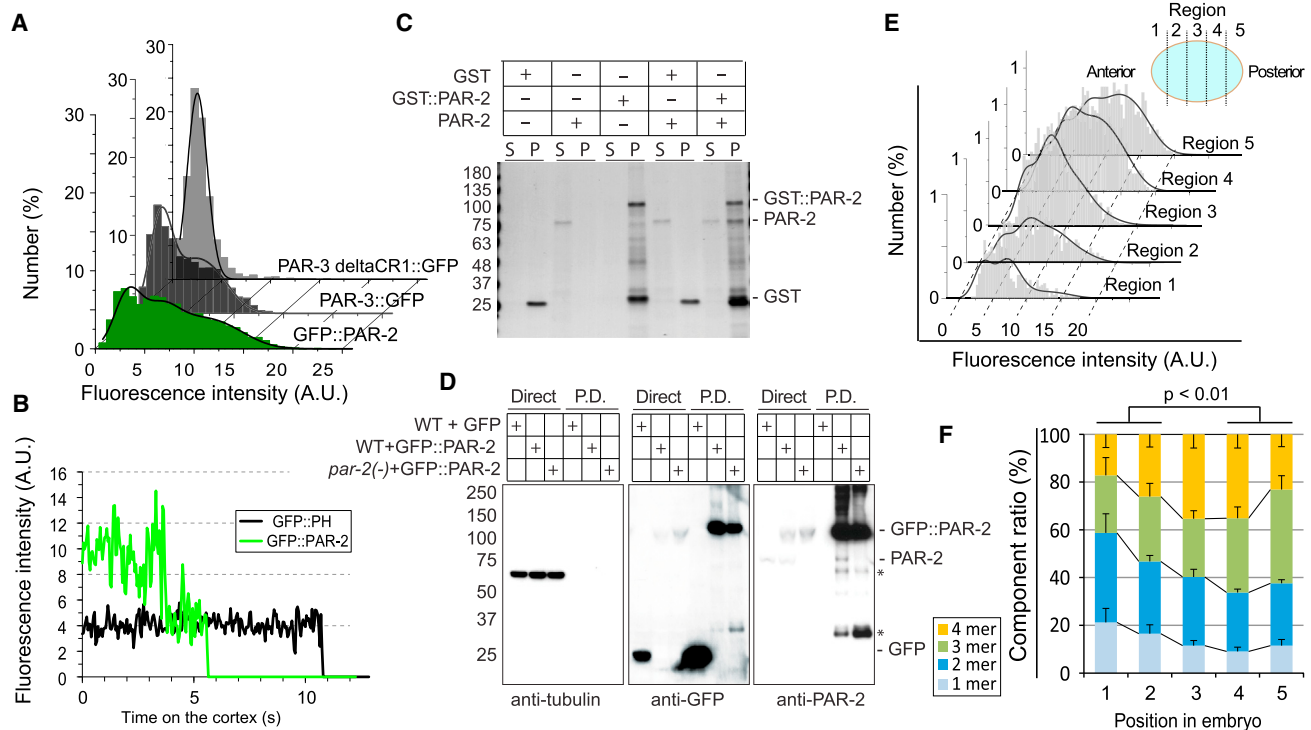
Figure 2. Oligomer-Size Asymmetry of Cortical PAR-2 along the A-P Axis

(A) Representative FI histograms obtained from the fluorescence intensity of GFP::PAR-2 particles on the cortex. Histogram fitting was performed using Gaussian mixture models (n_{max} = 4, 3, and 1 in Equation S1 for GFP::PAR-2, PAR-3::GFP, and PAR-3(ΔCR1)::GFP, respectively).

(B) Stepwise photobleaching of cortical particles.

(C) GST pull-down assay to test the homobinding character of PAR-2 using glutathione-conjugated agarose beads in vitro. S, supernatant fraction; P, precipitated fraction. Numbers on the left side of the gel indicate molecular weight markers. GST-PAR-2, PAR-2, and GST were detected by Coomassie staining.

(D) Immunoprecipitation using GFP-Trap beads to test the homobinding character of PAR-2 in vivo. Direct: direct worm lysate; P.D.: pull-down fraction. Numbers on the left side of the gel indicate molecular weight markers. Tubulin, GFP, and PAR-2 were detected by western blotting using their antibodies. Endogenous PAR-2 was precipitated from lysate collected from WT embryos expressing GFP::PAR-2 (WT+GFP::PAR-2), but not from *par-2* knockout embryos (*par-2* (–)+GFP::PAR-2). Asterisks indicate bands most likely due to the degradation product of GFP::PAR-2.

(E) Representative FI histograms of PAR-2 particles in five cortical regions along the a-p axis. Fitting was performed using a four-component Gaussian mixture model (n_{max} = 4 in Equation S1). Blue ellipse: schematic division of the *C. elegans* embryonic cortex into five equally spaced regions along the a-p axis.

(F) Mean percentages of oligomers (1- to 4-mer), determined by Equations S1 and S2, shown with SEM (error bars). Ratios of smaller (1- and 2-mer) and larger (3- and 4-mer) oligomers significantly differed between the anterior (1 and 2) and posterior (4 and 5) regions of the cortex (p < 0.01, t test).
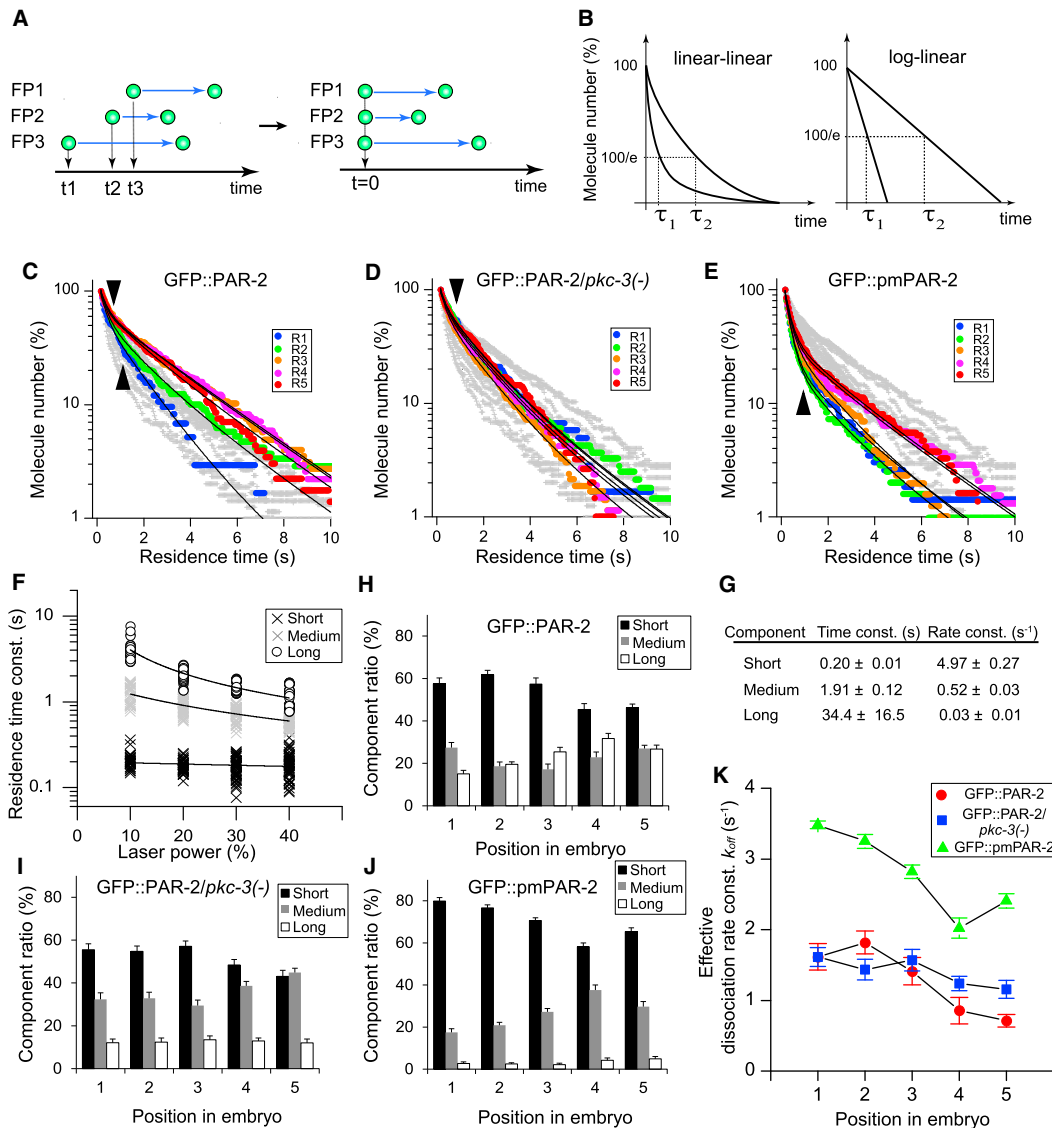
See also Figure S1.

The Effective Dissociation Rate Is Determined by the Collective Kinetics of Single PAR-2 Molecules

To study the spatial control of the PAR-2′s dissociation rate, we constructed release curves of PAR-2. In the release curve, the dissociation rate constant was obtained from the inverse of the residence time constant, which is the time period for 1/e (∼37%) of molecules to leave the cortex (Figures 3A and 3B; Supplemental Experimental Procedures). We found that release curves of GFP::PAR-2 in the anterior cortex decayed faster than those for the posterior cortex (Figure 3C). This a-p difference disappeared in GFP::PAR-2/*pkc-3*(–) (Figure 3D) but was reduced in GFP::pmPAR-2 (Figure 3E), confirming that phosphorylation plays a role in spatially controlling the rate asymmetry.

Most release curves exhibited clear inflection points in a semi-log plot representation (Figures 3C–3E), indicating that PAR-2 had multiple components with different dissociation rates. To

obtain the residence time constants and the relative ratios of the various PAR-2 species, we globally fit (Supplemental Experimental Procedures) the release curves with a three-component exponential decay model (n = 3 in Equation S3; Figures 3C–3E). The photobleaching effects on the apparent residence time of each component were removed by fitting the apparent time constant versus excitation laser power (Figure 3F) to an empirical function (Equation S4) and extrapolating the function to zero power. We found that photobleaching-corrected values varied from orders of 10^{-1} to 10^{1} s (Figure 3G; Supplemental Experimental Procedures).

In GFP::PAR-2, we found that the ratios of the long and short components (A_i in Equation S3), respectively, increased and decreased along the a-p axis (Figure 3H), appearing to plateau in the posterior (4 and 5) and anterior (1 and 2) regions of the cortex, respectively. In GFP::PAR-2/*pkc-3*(–), the asymmetry of the component ratio was abolished (Figure 3I). Interestingly,

Figure 3. Asymmetry of the Effective Dissociation Rate Constant of PAR-2 Due to the Ratio Control of Single PAR-2 Molecules with Different Rate Constants

(A) Schematic illustration of the construction of release curves from single-particle observations. In the left panel, time histories of three fluorescent PAR-2 particles (FP1, FP2, and FP3 shown by green circles) were obtained by particle tracking; a PAR-2 particle appears on the cortex at the various time points (t1, t2, and t3). After certain residence times (the blue arrow), a particle dissociates from the cortex. In these time history data in the left panel, the time point when the particle appears on the cortex is set as the zero time point (t = 0) in the right panel. The release curves were constructed by counting the number of fluorescent particles that remain on the cortex at a time, τ, after the zero time point. At the zero time point, 100% of particles reside on the cortex, and then the number of cortical particles decays exponentially according to the residence time as shown in (B).

(B) Schematic illustrations of the exponential decay processes observed via the release curves, shown in linear and semi-log plots. The residence time constants were shown by τ_1 or τ_2.

(C–E) Representative release curves in five cortical regions along the a-p axis. Curves were fit with a three-component exponential decay model (n = 3 in Equation S3). Arrowheads: inflection points of the release curves identified visually. Release curves are superimposed with gray crosses.

(F) Apparent residence time constants of short, medium, and long components obtained from 10%–40% laser powers were plotted as a function of excitation laser power. Fitting was performed with Equation S4.

(G) Photobleaching-corrected values of time and rate constants of short, medium, and long components, estimated by the fittings in (D) (mean ± SE of fitting).

(H–J) Ratios of short, medium, and long components in five regions along the a-p axis. Means are shown with SEM. The component ratios were affected by photobleaching during TIRF observation (Figure S1I). We used component ratio data obtained at 10% laser power as a photobleaching-minimized value (Figure S1I and Supplemental Experimental Procedures).

(K) Effective dissociation rate constants calculated from the contribution of the three components, plotted along the a-p axis. Means are shown with SEM were determined from reconstructed release curves.

See also Supplemental Experimental Procedures.

the component ratios remained asymmetric in GFP::pmPAR-2, but the relative ratio of the short component was significantly increased as compared to the other two components (Figure 3J). These results suggest that the component ratios of PAR-2 species are regulated by a PKC-3 phosphorylation-dependent mechanism.

To capture the essential kinetics of the PAR-2 dissociation in a single parameter, we introduced the effective dissociation rate constant. This rate constant was defined as the 1/e value of the release curves and was calculated from the photobleaching-corrected residence times and photobleaching-minimized component ratios (Figures 3G and 3H–3J; Supplemental Experimental Procedures). Plotted as a function of cortical position, the effective rate showed non-linear variation along the a-p axis in GPF::PAR-2 (Figure 3K). In comparison, for GFP::PAR-2/*pkc-3*(–), the effective rate did not change along the a-p axis. In GFP::pmPAR-2, the asymmetry remained, but the basal dissociation rate was higher than in GFP::PAR-2. The spatial changes to the 1/e effective rate are interpreted as the effect of modifying the ratios of short-time versus long-time residing cortical PAR-2 components. We propose that the component-ratio-weighted 1/e rate is physiologically relevant for polarity maintenance (see Discussion).

Dissociation Rate of Cortical PAR-2 Particles Varies with Oligomer Size and Phosphorylation Status

To study the molecular mechanisms generating PAR-2 species with different dissociation rates, we compared the rates under different conditions. For same-sized oligomers (Figures 4A and 4B), anteriorly localized PAR-2 dissociated faster than posteriorly localized PAR-2. Moreover, smaller oligomers appeared to dissociate faster than larger oligomers on either side of the cortex, raising the possibility that the cortical residence time is regulated both by PKC-3-dependent phosphorylation and PAR-2 oligomerization.

To confirm the effect of phosphorylation on residence time, we compared the time constants of GFP::pmPAR-2 and GFP::PAR-2/*pkc-3*(–). Regardless of oligomer size, GFP::pmPAR-2 dissociated faster than GFP::PAR-2/*pkc-3*(–) (Figures 4C and 4D), indicating that the residence time of cortical PAR-2 is regulated by PKC-3-dependent phosphorylation. To confirm the effect of PAR-2 oligomerization on residence time, we compared the photobleaching-corrected dissociation rates between small and large oligomers. We classified all the fluorescent particles separately into darker and brighter half fractions as a relative measure of small and large oligomers (Figure 4E). Although the darker fraction may contain a mix of small oligomers and large oligomers with photobleached GFP::PAR-2 molecules, the brighter fraction should contain a higher proportion of large oligomers. We obtained the photobleaching-corrected values by fitting the relationship between the time constant versus laser power using Equation S5, and extrapolating the function to zero power. The darker fraction dissociated faster than the brighter fraction both in GFP::pmPAR-2 and GFP::PAR-2/*pkc-3*(–) (Figures 4F and 4G), indicating that large oligomers exhibit a slower dissociation, whereas small oligomers exhibit a faster dissociation.

The above results suggest that a highly phosphorylated and smaller oligomer form of PAR-2 (Figure 4H) gives rise to a shorter residence time on the anterior cortex (Figure 3K), whereas a less-phosphorylated and larger oligomer form of PAR-2 (Figure 4H) gives rise to a longer residence time on the posterior cortex (Figure 3K). These results are supported by the fact that PKC-3 is cortically asymmetric (Tabuse et al., 1998) and the observation that the oligomer-size of PAR-2 is asymmetric along the a-p axis (Figures 2E and 2F). We only identified three components in the release curve analysis (Figures 3), but the number of possible combinations of oligomer size and phosphorylation state of PAR-2 is larger than the three component fractions. It is possible that some combinations of the molecular modifications result in similar dissociation rate constants for PAR-2 molecules. Although the exact relationship between the phosphorylation status/oligomer size (Figure 4H) and the three component fractions remains unclear (Figures 3), the results in Figure 4 suggest that the nonlinear variation of the effective PAR-2 dissociation rate (Figure 3) is controlled by the collective kinetics of single PAR-2 molecules with differing degrees of phosphorylation and oligomerization. We note that although the assembly or disassembly of PAR-2 oligomers on the cortex could change the residence time distributions, we found by SMI that most fluorescent spots do not assemble or disassemble on the cortex; therefore, they do not significantly affect the residence time distributions (Supplemental Experimental Procedures).

Association Rate of Cytoplasmic PAR-2 onto the Cortex Is Asymmetric along the A-P Axis via a PKC-3-Dependent Mechanism

To study the spatial control of the association of cytoplasmic PAR-2 with the cortex, we introduced the effective association rate constant ($\widehat{k}_{on}\chi^{-1}$ in Equation S6). This rate was determined using an FCS-measured concentration of cortical/cytoplasmic PAR-2 (Figures S2F and S3D), and the effective dissociation rate (Figure 3K), based on an approximation of local equilibrium for the exchange of PAR-2 between the cortex and cytoplasm (Equation S6). This approximation is plausible because the lateral protein fluxes on the cortex/cytoplasm that could change the PAR-2 distribution are negligible (Supplemental Experimental Procedures). We found that effective association rate of GFP::PAR-2 varied along the a-p axis. The values of GFP::PAR-2/*pkc-3*(–) (or GFP::pmPAR-2) were as large as (as small as) those of GFP::PAR-2 on the posterior (anterior) cortex of WT embryos (Figure 5A). Using SMI, we confirmed the asymmetry of the association rates by counting the number of fluorescent molecules that appeared on the cortex per unit area per unit time (Supplemental Experimental Procedures). The appearance frequency of fluorescent PAR-2 molecules along the a-p axis was asymmetric in GFP::PAR-2, uniform in GFP::PAR-2/*pkc-3*(–), and weakly asymmetric in GFP::pmPAR-2 (Figures 5B and 5C). Thus, the effective association rate is consistent with the SMI-determined association rate. These results indicate that the association rate of PAR-2 also varies along the a-p axis in a PKC-3-dependent manner. We note that the cortical density of GFP::pmPAR-2 was lower than that of GFP::PAR-2 (Figure S3D), despite the higher expression levels of GFP::pmPAR-2 as compared to GFP::PAR-2 (Figure 1A). This observation suggests that the lower association rate of GFP::pmPAR-2 is not likely due
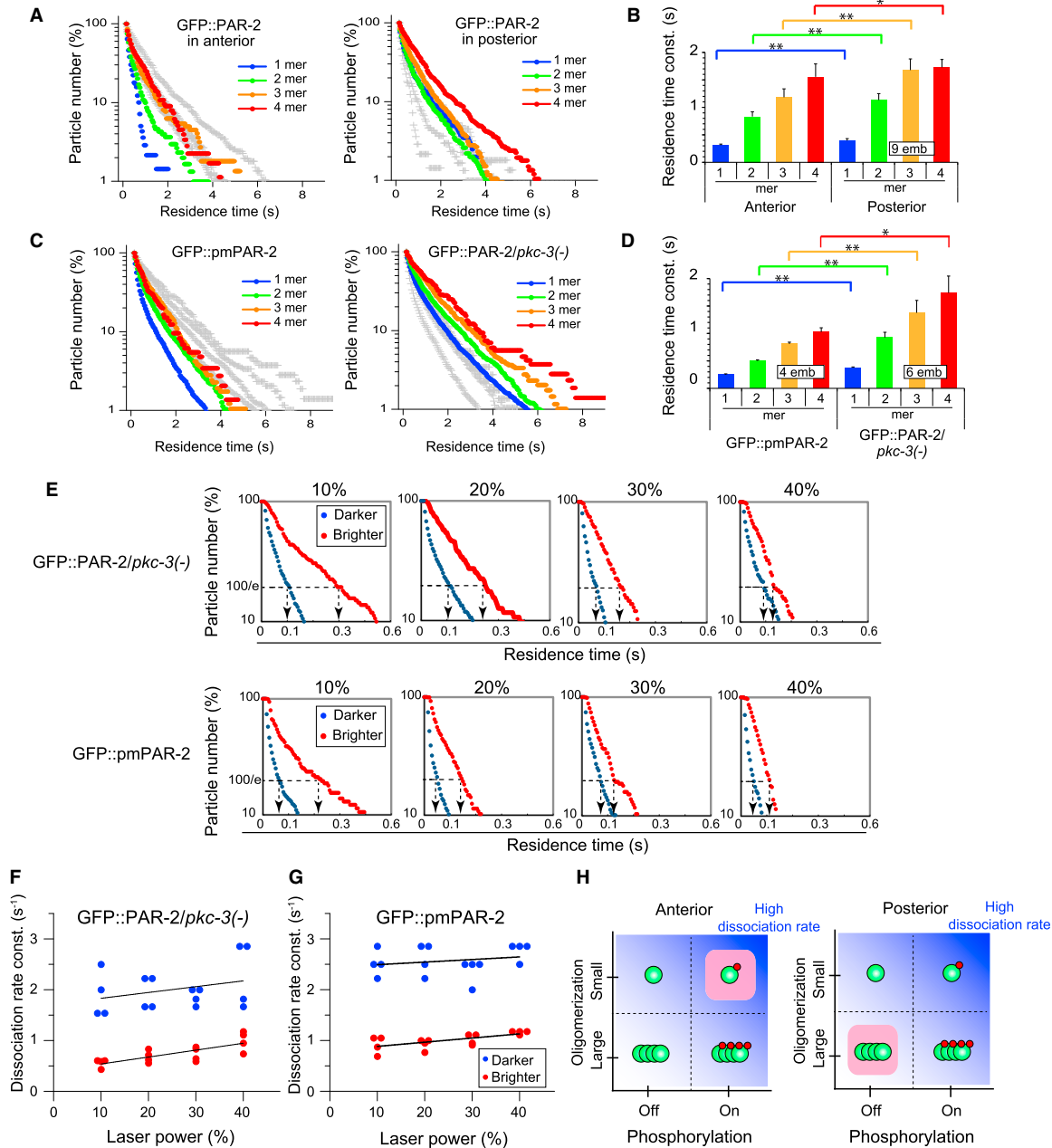
Figure 4. Dissociation Rate Constants of Single PAR-2 Particles in Accordance with Phosphorylation and Oligomerization of PAR-2

(A–D) Release curves (A and C) and residence time constants (B and D) of anterior and posterior cortical particles of GFP::PAR-2, and of cortical particles of GFP::PAR-2/*pkc-3*(–) and GFP::pmPAR-2, for each oligomer size. Release curves are superimposed with gray crosses. Oligomer size was determined by dividing the region between the weaker and stronger tail ends in the FI into four regions. The means of the residence time constants were obtained from the indicated numbers of embryos (emb) are shown with SEM. *p < 0.05, **p < 0.01 by t test.

(E) Release curves of cortical particles of GFP::PAR-2/*pkc-3*(–) and GFP::pmPAR-2, for brighter and darker fluorescent particles. Particles were separated by their position in the FI histogram.

(F and G) Apparent dissociation rate constants of brighter and darker fluorescent particles, plotted as a function of excitation laser power. Estimated rate constants of brighter and darker fluorescent particles were 0.40 ± 0.08 s^{-1} and 1.7 ± 0.3 s^{-1} in GFP::PAR-2/*pkc-3*(–), and 0.80 ± 0.07 and 2.4 ± 0.2 s^{-1} in GFP::pmPAR-2, respectively, in each case (mean ± SE of fitting by Equation S5). Photobleaching-corrected values of brighter and darker fluorescent particles differed (p < 3×10^{-4} and p < 2×10^{-8} for GFP::PAR-2/*pkc-3*(–) and GFP::pmPAR-2, respectively; t test for regression intercepts).

(H) Dissociation rate constants of PAR-2 from the cortex were varied in accordance with the two mechanisms (phosphorylation and oligomerization). Green circles connected to a small red circle and multiple green circles indicate phosphorylated and oligomerized PAR-2 proteins, respectively. The blue gradient area indicates a higher dissociation rate. Light-red-shaded areas of the square indicate that a less-oligomerized and highly phosphorylated form of PAR-2 and a highly oligomerized and less-phosphorylated form of PAR-2 are enriched on the anterior and posterior cortex, respectively.
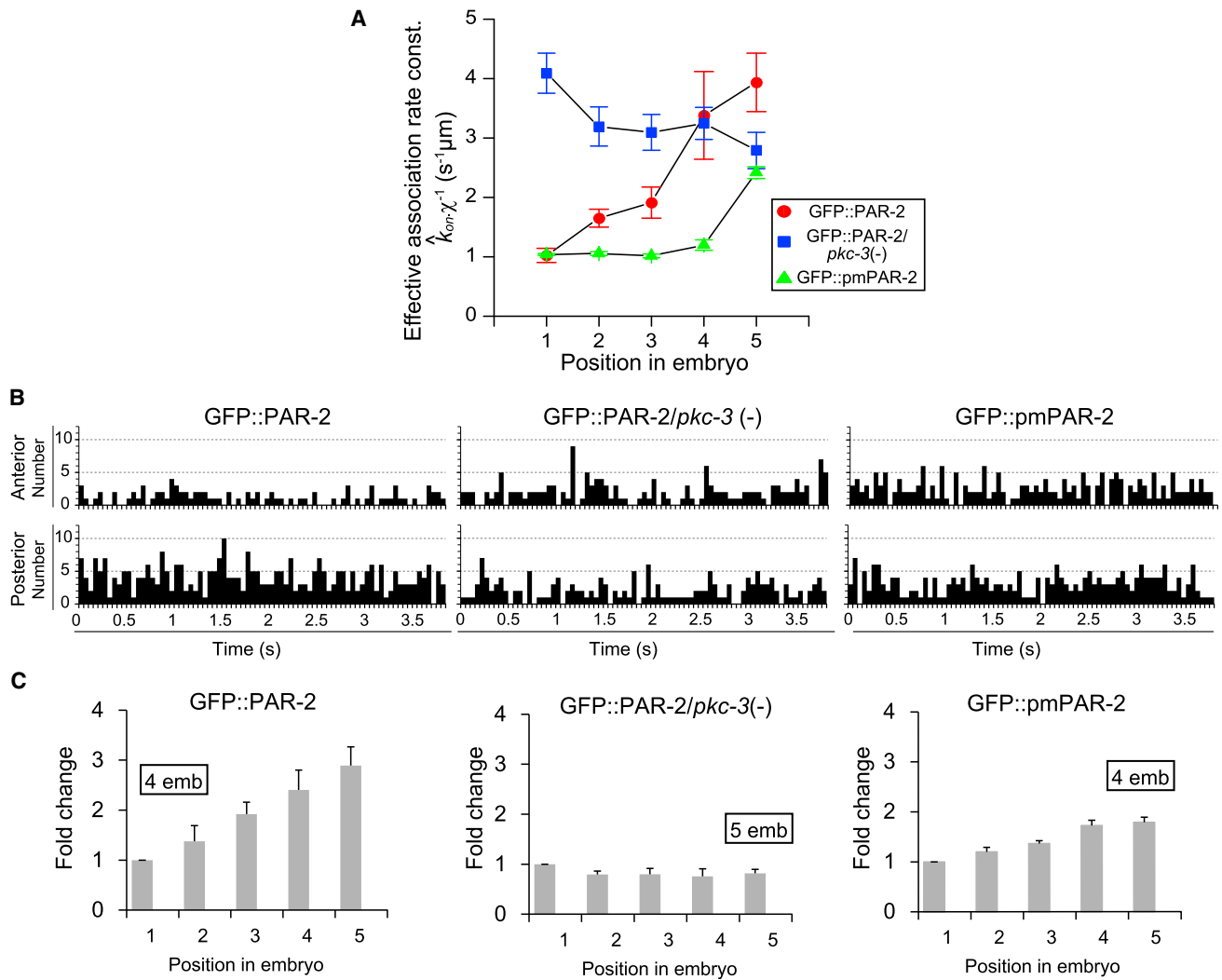
Figure 5. Asymmetry of Association Rate Constants along the A-P Axis in a PKC-3-Dependent Mechanism
(A) Effective association rate constants along the a-p axis, determined by Equation S6.
(B) Appearance frequencies of fluorescent particles on the cortex, compared between the anterior and posterior regions. Shown are the numbers of fluorescent particles that appeared on the cortex in a unit area per unit time.
(C) Relative appearance frequencies of PAR-2 molecules along the a-p axis. Appearance frequencies were normalized to the frequency in region 1. Means obtained from the indicated numbers of embryos (emb) are shown with SEM (error bars).
See also Figures S2 and S3 and Supplemental Experimental Procedures.

to saturation of the putative receptor of PAR-2 that mediates cortical association (see Discussion).

The Cortical-Cytoplasmic Exchange Rates Control the Biphasic PAR-2 Distribution

To test whether our experimental measurements of PAR-2 diffusion and cortical binding kinetics were sufficient to explain cortical protein patterning, we used a reaction-diffusion model. We modeled cortical and cytoplasmic concentration in one dimension along the a-p axis with periodic boundary conditions (Figure S4A), as defined in Equations S7 and S8. To simplify the mutual exclusion in the PAR/aPKC system, we made an assumption that the mutual inhibition between anterior and pos-

terior PAR proteins can be described by a self-feedback loop for PAR-2 (Figure S4B). Mathematically, for two factors X and Y, we modify the mutual inhibition (X inhibits Y, and Y inhibits X) into a simpler, but equivalent, problem (X inhibits X through Y via a kinetic rate function). Thus, the rate constant of PAR-2 was described as a function of its own cortical density as a rate density function (RDF). The RDF includes the multistep and indirect molecular reactions that regulate PAR-2 through the anterior PAR proteins (see Figure S4B for the details).

To empirically determine the RDFs, we employed a two-step approach (Supplemental Experimental Procedures). First, we determined the empirical relationship between the rate constants (R) and the relative fluorescence intensity (FI) of cortical

Table 1. Summary of Parameters Determined by In Vivo Measurements

Variable	Units	GFP::PAR-2	GFP::PAR-2/pkc-3(–)	GFP::pmPAR-2
V_{off}	s^{-1}	1.19 ± 0.226	0	1.51 ± 0.50
K_{mFI}	—	689 ± 84	0	514 ± 58
K_m^*	$nmol/10^{15}\mu m^2$	489 ± 59	0	321 ± 36
n_h	—	5.86 ± 4.34	1	11.1 ± 4.60
c_{off}	s^{-1}	0.53 ± 0.21	1.37 ± 0.13	2.05 ± 0.28
V_{on}	$s^{-1} nM^{-1}$	$(3.15 \pm 1.06) \times 10^{-3}$	0	$(1.95 \pm 1.19) \times 10^{-3}$
c_{onFI}	$s^{-1}\mu m$	0.494 ± 0.366	3.25 ± 0.20	0.241 ± 0.509
c_{on}^*	$s^{-1}\mu m$	1.124 ± 0.366	3.25 ± 0.20	0.615 ± 0.509
D_m	$\mu m^2 s^{-1}$	0.05 ± 0.01	0.06 ± 0.02	0.05 ± 0.01
D_c	$\mu m^2 s^{-1}$	4.6 ± 0.3	5.0 ± 0.7	5.3 ± 0.2
$[PAR\text{-}2_{avg}]_m$	$nmol/10^{15}\mu m^2$	501 ± 191	422 ± 14	373 ± 101
$[PAR\text{-}2_{avg}]_c$	nM	206 ± 4	180 ± 5	719 ± 8

V_{off}, n_h, c_{off}, K_{mFI}, V_{on}, and c_{onFI} were obtained from the fitting of the empirical R-FI relationships (Figures 6A and 6B; Supplemental Experimental Procedures). K_m^* and c_{on}^* in GFP::PAR-2 and GFP::pmPAR-2 were obtained from K_{mFI} and c_{onFI} using the empirical relationship between cortical FI and FCS-determined cortical density of PAR-2 (Figure S4C; Supplemental Experimental Procedures). Diffusion coefficients (D_m and D_c) and mean concentrations ($[PAR\text{-}2_{avg}]_m$ and $[PAR\text{-}2_{avg}]_c$) were obtained from Figures 1D, S2G, S2F, and S3D. V_{off}, n_h, c_{off}, K_m^*, V_{on}, c_{on}^*, D_m, D_c, $[PAR\text{-}2_{avg}]_m$, and $[PAR\text{-}2_{avg}]_c$ were used for simulations (Figures 6 and S4). Data in dissociation RDFs are shown with the SD. Data in association RDFs are shown with the SE of fitting. Values without error values indicate fixed values in the fitting process.
See also Table S1 for the units and meanings of the parameters indicated.

PAR-2 measured from confocal images (the R-FI relationship). Then, using the empirical relationship between cortical FI and cortical density (Figure S4C), we transformed the R-FIs by converting the fluorescence intensity in the R-FI relationship to a cortical density to obtain RDFs. This two-step approach was used to ensure that the RDF curve maintained the correct shape and scaling relationships between the rates and cortical PAR-2 density. The estimated dissociation R-FI functions of GFP::PAR-2 and GFP::pmPAR-2 were nonlinear and hence ultrasensitive to the cortical density variations (n_h = 5.9 and 11 for GFP::PAR-2 and GFP::pmPAR-2; Table 1; Figure 6A), and the association R-FI function of GFP::PAR-2 had higher sensitivity to the cortical PAR-2 density variation than GFP::pmPAR-2 (Table1; Figure 6B). Due to the lack of dependency on cortical density, both the association and dissociation R-FIs for GFP::PAR-2/pkc-3(–) were fit as constants (Figures 6A and 6B). As well, in addition to the RDFs, we experimentally obtained all the parameters describing cortical and cytoplasmic diffusion (Figures 1D and S2G) and the average density/concentration of PAR-2 (Figures S2F and S3D) using SMD technologies (Table 1).

These experimentally obtained values were used as the parameters in the reaction-diffusion equations (Equations S7 and S8) and the concentration conservation law (Equation S9), leaving no free parameters (Table 1). Numerically solving the equations for PAR-2 cortical and cytoplasmic density, we found that biphasic distributions at the steady state were obtained for both the GFP::PAR-2 and GFP::pmPAR-2 models: a low-density region (on the anterior cortex) was separated by a steep boundary from a high-density region (on the posterior cortex) (Figure 6C). Meanwhile, the cortical distribution remained uniform with the PAR-2/pkc-3(–) model (Figure 6C). In all cases, the models produced a uniform cytoplasmic concentration of PAR-2 along the a-p axis (Figure 6D). Thus, the mathematical PAR-2 spatial distributions were qualitatively consistent with

the in vivo biphasic spatial distribution exhibited by PAR-2 (Figures 1A and 6E) and many other polarity proteins (Nishimura et al., 2004; Mayer et al., 2005; Goehring et al., 2011a; Orlando et al., 2011; Shibata et al., 2012). These results suggest that our SMD identified PAR-2 components are sufficient for maintaining the cortical asymmetry.

To reveal the mechanism of maintenance, we studied the steady state of the theoretical models. The steady-state analysis indicated that the GFP::PAR-2 and GFP::pmPAR-2 systems maintain the cortical asymmetry via a bistable mechanism, and the system loses the bistability in GFP::PAR-2/pkc-3(–) (Figure S4D). By studying the relationship of the GFP::PAR-2 system with the GFP::PAR-2/pkc-3(–) or GFP::pmPAR-2 systems in the steady state (Figure S4E), we found that the loss of bistability in GFP::PAR-2/pkc-3(–) may be due to the loss of the nonlinear control of dissociation rates and/or caused by a higher basal association rate. The weak cortical asymmetry in GFP::pmPAR-2 is likely caused by a higher basal dissociation rate constant and/or a less sensitive linear control of the association rate. These results suggest that the bistability is achieved by a balanced control of the dissociation and association rates by a PKC-3-dependent mechanism. Altogether, our in vivo SMD measurements and mathematical modeling provide an integrated view of how spatial protein patterning at the cell scale emerges from modifications of polarity proteins at the single-molecule scale.

DISCUSSION

In Vivo Quantitative Measurements of PAR-2 and Mathematical Modeling
Spatial and temporal dynamics of the PAR protein distribution during the establishment and maintenance of asymmetric localization have been discussed in many mathematical models
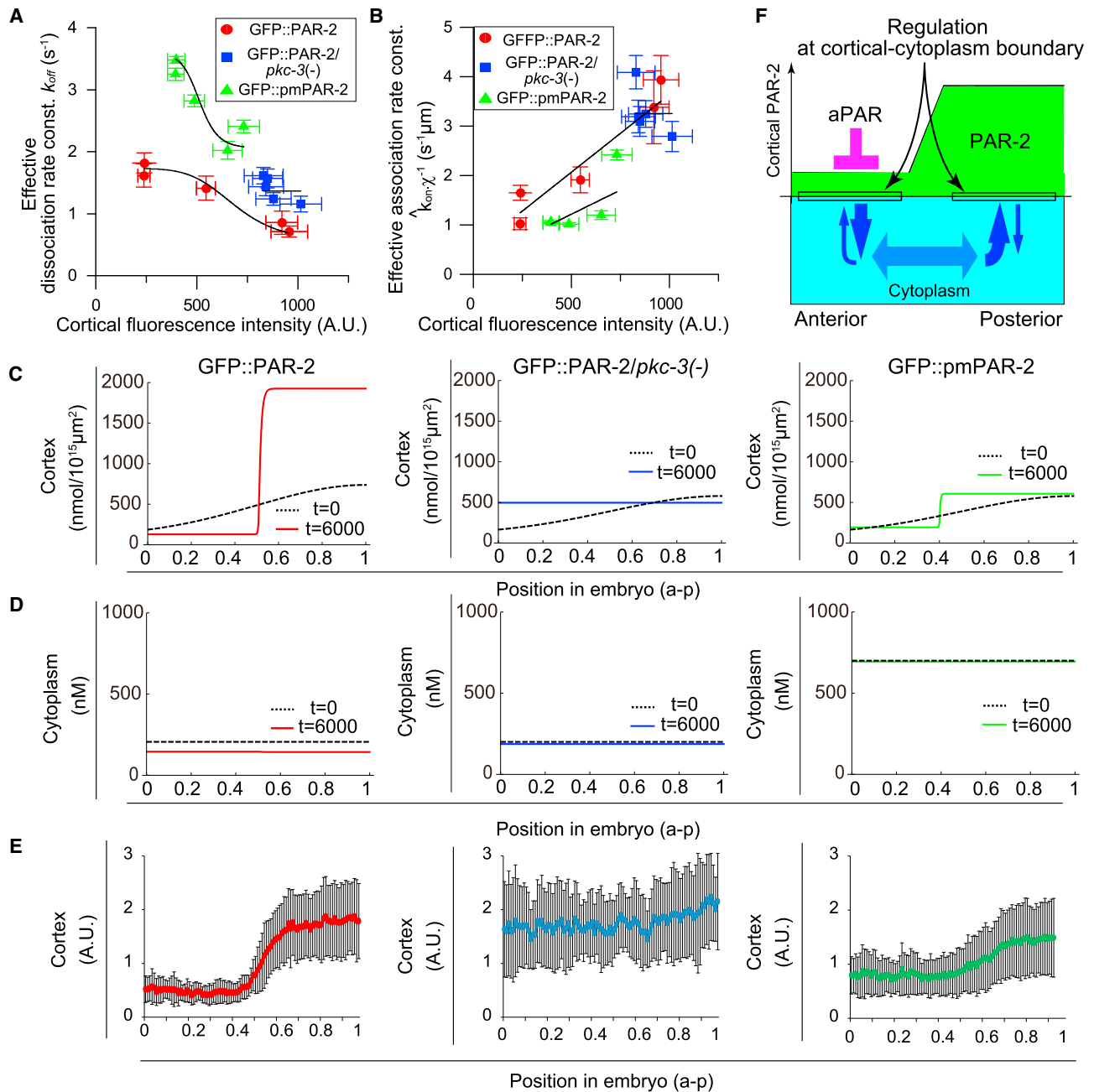
Figure 6. The Cortical-Cytoplasmic Exchange Reproducing the Biphasic Distribution of PAR-2

(A and B) Effective values of the dissociation (A) and association (B) rate constants as a function of the FI of cortical PAR-2. Means and SEMs (error bars) in the y axis are from Figures 3K and 5A. Data in the x axis are from Figure 6E. Fitting was performed with a Hill function (Equation S10) (A) or linear function (Equation S11) (B) through a bootstrapping method (Supplemental Experimental Procedures).

(C and D) Cortical and cytoplasmic distributions of PAR-2 in numerical simulations. Dashed lines ($t = 0$ s): initial distribution. Solid colored lines ($t = 6000$ s): steady-state distribution.

(E) Quantification of protein distribution on the cortex of embryos from confocal images. Average and SD of cortical PAR-2 were obtained from 15, 17, and 19 embryos, respectively.

(F) Schematic illustration of maintenance of PAR-2 asymmetry. Asymmetric PAR-2 localization is maintained by controlling the ratio of supply (upward blue arrows) and removal rate (downward blue arrows) at most of the cortical-cytoplasmic boundary along the a-p axis (two black squares). Most PAR-2 that appears on the cortex dissociates from the same cortical side (i.e., the long unshaded rectangles in the anterior and posterior regions). Cytoplasmic protein diffuses a much longer distance that cortical PAR-2 (horizontal blue arrows). The thickness of blue arrows corresponds to the rate constant. Especially, anterior PAR proteins eliminate PAR-2 that is supplied from the anterior cytoplasm on the cortex (magenta).

See also Figure S4, Tables 1 and S1, and Supplemental Experimental Procedures.

(Tostevin and Howard, 2008; Dawes and Munro, 2011; Goehring et al., 2011b; Sailer et al., 2015). In these models, the protein dynamics were reproduced based on free parameters or partially on values obtained by quantitative in vivo measurements using FRAP. Due to the assumptions in these models, it was still unclear how molecular-level modifications affected intracellular protein dynamics, and how the changes in the PAR dynamics achieved polarity maintenance in vivo. In this study, we used a parameter-free mathematical model to test whether our quantitative in vivo measurements were sufficient to reproduce the cortical PAR-2 asymmetry. When a two-component model was used to fit the release curve data, the asymmetric localization could not be reproduced due to insufficient nonlinear variation of the effective dissociation rate. However, by including a third component in the dissociation RDF, we succeeded in reproducing the cortical asymmetric localization. The third, short component, exhibited unexpectedly short residence times (Figure 3G), and this component is unlikely to be an artifact of over-parametrization (Supplemental Experimental Procedures).

Our measurements of GFP::PAR-2 dynamics are consistent with previously measured results based on FRAP (Goehring et al., 2010; Goehring et al., 2011a) and further extend their range. In the previous FRAP measurements, the fluorescence recovery curves were fit with a single-component model and identified a PAR-2 component with dissociation rate constant ($\sim$0.01 s^{-1}). Using SMI, we took advantage of measurements of faster protein dynamics and the ability to dissect contributions of individual molecules to identify two other components (short and medium) using a multiple-component model in fitting (Figures 3C–3E). The combination of a longer signal-acquisition time and ensemble averaging of all molecule contributions by a single-component fit can explain why FRAP did not identify these faster components. We suggest that the long component in our study ($\sim$0.03 s^{-1}) is likely identical to the FRAP-identified component measured previously ($\sim$0.01 s^{-1}) (Goehring et al., 2011a), whereas the short and medium components ($\sim$5 s^{-1} and 0.5 s^{-1}) are components identified here for PAR-2.

To further explain the difference between our SMI and FRAP measurements, we note a difference in the definition of the dissociation rate. Ensemble/time-averaging techniques such as FRAP intrinsically measure the time-weighted expectation-value rate, which comes from an ensemble/time averaging calculation. SMI can measure the expectation-value rate and the component-ratio-weighted 1/e value effective rate. For a single-component system, both definitions are equivalent, but for a multi-component system (Figures 3C–3E) they differ. Our 1/e-value rate was intermediate between the short and long components (Figure 3K; $\sim$1 s^{-1}) and exhibited a nonlinear variation along the polarity axis, whereas the expectation-value rate exhibited a more uniform distribution along the polarity axis due to the time-weighting influence of the long-residing cortical component ($\sim$0.1 s^{-1}, data not shown); the latter was closer to the FRAP-determined value ($\sim$0.01 s^{-1}) (Goehring et al., 2011a).

To argue that the 1/e-value is more physiologically relevant for polarity maintenance, we separately used both sets of values in our mathematical model. With the 1/e-value rate, we succeeded in reproducing the asymmetric PAR-2 localization due to the nonlinear variation of the dissociation rate, whereas we did not reproduce the asymmetry with the expectation-value effective rate due to insufficient nonlinearity. This result suggests that the dynamics of multiple PAR-2 components together can achieve the cortical asymmetry, but a long-residing component in isolation is not sufficient. Moreover, the effective dissociation rate derived from the 1/e definition was consistent with the effective association rate (Figure 5). In total, we comprehensively determined PAR-2 protein dynamics in living embryos and reproduced asymmetric cortical localization in silico. This study reports a successful implementation of a mathematical model of cell polarization based on comprehensive measurements of in vivo protein dynamics.

Molecular Mechanisms for the Dissociation Rate Control of PAR-2 from the Cortex

Previous mathematical models have assumed that the rate constants of PAR proteins are nonlinearly varied due to molecular modifications (Dawes and Munro, 2011; Goehring et al., 2011b; Sailer et al., 2015). However, how the nonlinear dynamics were achieved by the molecular modifications was unclear. We found that the source of nonlinear dissociation rate control was the 1/e effective rate kinetics of different PAR-2 species, which arises from molecular modifications to PAR-2.

Our direct measurement of individual proteins using SMI confirmed a model in which the phosphorylation of PAR-2 by PKC-3 regulates PAR-2 dissociation from the cortex (Cuenca et al., 2003; Hao et al., 2006), and we suggest PAR-2 oligomerization as a mechanism for controlling the dissociation rate. It is possible that phosphorylation and oligomerization of PAR-2 affects the dissociation rate by adding negative electrostatic charges to the protein surface due to a phosphoryl group (Motegi et al., 2011) and by simultaneous binding of multiple PAR-2 proteins to the cortical receptor for PAR-2, respectively. Additionally, we found that phosphorylation of PAR-2 by PKC-3 is required to establish the spatial oligomer-size asymmetry. It has been shown that phosphorylation of PAR-3 by PAR-1 blocks PAR-3 oligomerization (Benton and St Johnston, 2003b); thus, our finding raises the possibility that cortical residence times of PAR-2 and PAR-3 are regulated by kinase-dependent oligomer-size regulation along the polarity axis in the PAR/aPKC system. It is possible that oligomerization and phosphorylation occur in a cooperative manner. For instance, oligomerization could be inhibited by multistep phosphorylation at multiple PKC-3 sites in PAR-2 (e.g., by inducing conformational changes), whereas phosphorylation may be inhibited by oligomerization (e.g., by masking PKC-3 sites on PAR-2). Our measurements also suggest that another unknown mechanism under the control of PAR polarity may regulate dissociation rates of PAR-2 (Supplemental Experimental Procedures). Thus, we surmise that the nonlinear dissociation rate control of PAR-2 may be achieved by the mutual interaction of multiple molecular mechanisms.

Molecular Mechanisms for the Association Rate Control of PAR-2 on the Cortex

The PAR-2 association rate was considered to be constant along the a-p axis in the maintenance phase (Goehring et al., 2010, 2011a, 2011b; Dawes and Munro, 2011). However, it

has recently been reported that the recruitment rate of PAR-6 is asymmetric and the asymmetry is promoted by cortical localization of PAR-3 and active CDC-42 as cortical receptors (Robin et al., 2014; Sailer et al., 2015). In this study, we found that the PAR-2 association rate is asymmetric due to a PKC-3-dependent mechanism. This asymmetry may also depend on the spatial distribution of a cortical receptor for PAR-2. An enzyme involving lipid metabolism in the cortical membrane, phosphatidylinositol-4-phosphate 5′ kinase (PPK-1) is known to localize to the posterior cortex in a PAR-dependent manner (Panbianco et al., 2008). As PAR-2 directly binds to phosphatidylinositol lipids (Motegi et al., 2011), the putative asymmetric distribution of these lipids may account for the asymmetry of the PAR-2 association rate. In addition, cortical PAR-2 may function as a receptor through direct assembly with cytoplasmic PAR-2 to form a larger oligomer on the posterior cortex. On the anterior cortex, phosphorylated cortical PAR-2 may have a lower affinity for direct assembly with cytoplasmic PAR-2. These results suggest that there may be a feedback mechanism between the putative cortical receptor and cortical PAR proteins.

Polarity Is Maintained by the Kinetic Control of PAR-2 Exchange at the Boundary between the Cortex and Cytoplasm

It has been proposed that the PAR density equalizing effects of cortical diffusion are counteracted by affinity differences of the PAR proteins between the anterior and posterior domains. (Goehring et al., 2011a). It remained unclear from previous studies whether the cortical asymmetry was maintained by promoting dissociation of PAR-2 molecules that invaded the anterior cortex by cortical diffusion, or by inhibiting the association of molecules to the anterior cortex from the cytoplasm. We found that the distance of cortical diffusion of PAR-2 (determined by $\sqrt{2D\tau}$; D, diffusion coefficient; τ, residence time constant; ~0.1, ~0.4, and ~1.9 μm for short, medium, and long components, respectively) was less than 10% of the length of the polarity axis (30–50 μm). The FRAP-determined diffusion distance of PAR-2 in WT embryos (4.2 μm, calculated from $D_m = 0.09$ μm^2/s and $\tau = 100$ s) (Goehring et al., 2011a) was also ~10% of the polarity axis length. Therefore, it is likely that for cortical PAR-2 molecules residing in the central 10% of the embryo, asymmetry is maintained by the polarity-boundary mutual exclusion mechanism, whereas PAR-2 on the other 90% of the cortical area is regulated by the exchange kinetics at the cortical-cytoplasmic boundary.

To account for differences in diffusion distances measured by SMI and FRAP, we cannot exclude the possibility that SMI underestimates the diffusion distances or preclude the existence of a component with longer residence time than the long component (Supplemental Experimental Procedures). However, our SMI measurements identified a sufficient set of PAR-2 components to account for the cortical asymmetry. So even if "longer" components are present, they likely play an auxiliary function for the cortical asymmetry. Thus, we conclude that the cortical PAR-2 asymmetry is maintained largely by the local control of exchange kinetics at the cortical-cytoplasmic boundary.

EXPERIMENTAL PROCEDURES

Conditions of *C. elegans* Embryos for SMI and FCS

SMI and FCS measurements were completed during the maintenance phase of the one-cell embryo, which is the time period between the completion of pseudocleavage and the initiation of cell cleavage. Under the conditions, asymmetric localization of PAR-2 was maintained, and the one-cell embryos initiated cell cleavage.

SUPPLEMENTAL INFORMATION

Supplemental Information includes Supplemental Experimental Procedures, thirteen equations, four figures, one table, and three movies and can be found with this article online at http://dx.doi.org/10.1016/j.celrep.2016.07.047.

REFERENCES

Audhya, A., Hyndman, F., McLeod, I.X., Maddox, A.S., Yates, J.R., 3rd, Desai, A., and Oegema, K. (2005). A complex containing the Sm protein CAR-1 and the RNA helicase CGH-1 is required for embryonic cytokinesis in *Caenorhabditis elegans*. J. Cell Biol. *171*, 267–279.

Beatty, A., Morton, D.G., and Kemphues, K. (2013). PAR-2, LGL-1 and the CDC-42 GAP CHIN-1 act in distinct pathways to maintain polarity in the *C. elegans* embryo. Development *140*, 2005–2014.

Benton, R., and St Johnston, D. (2003a). A conserved oligomerization domain in *drosophila* Bazooka/PAR-3 is important for apical localization and epithelial polarity. Curr. Biol. *13*, 1330–1334.

Benton, R., and St Johnston, D. (2003b). *Drosophila* PAR-1 and 14-3-3 inhibit Bazooka/PAR-3 to establish complementary cortical domains in polarized cells. Cell *115*, 691–704.

Boyd, L., Guo, S., Levitan, D., Stinchcomb, D.T., and Kemphues, K.J. (1996). PAR-2 is asymmetrically distributed and promotes association of P granules and PAR-1 with the cortex in *C. elegans* embryos. Development *122*, 3075–3084.

Cuenca, A.A., Schetter, A., Aceto, D., Kemphues, K., and Seydoux, G. (2003). Polarization of the *C. elegans* zygote proceeds via distinct establishment and maintenance phases. Development *130*, 1255–1265.

Dawes, A.T., and Munro, E.M. (2011). PAR-3 oligomerization may provide an actin-independent mechanism to maintain distinct par protein domains in the early *Caenorhabditis elegans* embryo. Biophys. J. *101*, 1412–1422.

OPEN
ACCESS
CellPress

Goehring, N.W., Chowdhury, D., Hyman, A.A., and Grill, S.W. (2010). FRAP analysis of membrane-associated proteins: lateral diffusion and membrane-cytoplasmic exchange. Biophys. J. 99, 2443–2452.

Goehring, N.W., Hoege, C., Grill, S.W., and Hyman, A.A. (2011a). PAR proteins diffuse freely across the anterior-posterior boundary in polarized C. elegans embryos. J. Cell Biol. 193, 583–594.

Goehring, N.W., Trong, P.K., Bois, J.S., Chowdhury, D., Nicola, E.M., Hyman, A.A., and Grill, S.W. (2011b). Polarization of PAR proteins by advective triggering of a pattern-forming system. Science 334, 1137–1141.

Goldstein, B., and Macara, I.G. (2007). The PAR proteins: Fundamental players in animal cell polarization. Dev. Cell 13, 609–622.

Hachet, O., Berthelot-Grosjean, M., Kokkoris, K., Vincenzetti, V., Moosbrugger, J., and Martin, S.G. (2011). A phosphorylation cycle shapes gradients of the DYRK family kinase Pom1 at the plasma membrane. Cell 145, 1116–1128.

Hao, Y., Boyd, L., and Seydoux, G. (2006). Stabilization of cell polarity by the C. elegans RING protein PAR-2. Dev. Cell 10, 199–208.

Hoege, C., and Hyman, A.A. (2013). Principles of PAR polarity in Caenorhabditis elegans embryos. Nat. Rev. Mol. Cell Biol. 14, 315–322.

Hoege, C., Constantinescu, A.T., Schwager, A., Goehring, N.W., Kumar, P., and Hyman, A.A. (2010). LGL can partition the cortex of one-cell Caenorhabditis elegans embryos into two domains. Curr. Biol. 20, 1296–1303.

Kozubowski, L., Saito, K., Johnson, J.M., Howell, A.S., Zyla, T.R., and Lew, D.J. (2008). Symmetry-breaking polarization driven by a Cdc42p GEF-PAK complex. Curr. Biol. 18, 1719–1726.

Li, B., Kim, H., Beers, M., and Kemphues, K. (2010). Different domains of C. elegans PAR-3 are required at different times in development. Dev. Biol. 344, 745–757.

Marco, E., Wedlich-Soldner, R., Li, R., Altschuler, S.J., and Wu, L.F. (2007). Endocytosis optimizes the dynamic localization of membrane proteins that regulate cortical polarity. Cell 129, 411–422.

Mayer, B., Emery, G., Berdnik, D., Wirtz-Peitz, F., and Knoblich, J.A. (2005). Quantitative analysis of protein dynamics during asymmetric cell division. Curr. Biol. 15, 1847–1854.

Mizuno, K., Suzuki, A., Hirose, T., Kitamura, K., Kutsuzawa, K., Futaki, M., Amano, Y., and Ohno, S. (2003). Self-association of PAR-3-mediated by the conserved N-terminal domain contributes to the development of epithelial tight junctions. J. Biol. Chem. 278, 31240–31250.

Motegi, F., Zonies, S., Hao, Y., Cuenca, A.A., Griffin, E., and Seydoux, G. (2011). Microtubules induce self-organization of polarized PAR domains in Caenorhabditis elegans zygotes. Nat. Cell Biol. 13, 1361–1367.

Nishimura, T., Kato, K., Yamaguchi, T., Fukata, Y., Ohno, S., and Kaibuchi, K. (2004). Role of the PAR-3-KIF3 complex in the establishment of neuronal polarity. Nat. Cell Biol. 6, 328–334.

Orlando, K., Sun, X., Zhang, J., Lu, T., Yokomizo, L., Wang, P., and Guo, W. (2011). Exo-endocytic trafficking and the septin-based diffusion barrier are required for the maintenance of Cdc42p polarization during budding yeast asymmetric growth. Mol. Biol. Cell 22, 624–633.

Panbianco, C., Weinkove, D., Zanin, E., Jones, D., Divecha, N., Gotta, M., and Ahringer, J. (2008). A casein kinase 1 and PAR proteins regulate asymmetry of a PIP(2) synthesis enzyme for asymmetric spindle positioning. Dev. Cell 15, 198–208.

Robin, F.B., McFadden, W.M., Yao, B., and Munro, E.M. (2014). Single-molecule analysis of cell surface dynamics in Caenorhabditis elegans embryos. Nat. Methods 11, 677–682.

Sailer, A., Anneken, A., Li, Y., Lee, S., and Munro, E. (2015). Dynamic Opposition of Clustered Proteins Stabilizes Cortical Polarity in the C. elegans Zygote. Dev. Cell 35, 131–142.

Sako, Y. (2006). Imaging single molecules in living cells for systems biology. Mol. Syst. Biol. 2, 56.

Shibata, T., Nishikawa, M., Matsuoka, S., and Ueda, M. (2012). Modeling the self-organized phosphatidylinositol lipid signaling system in chemotactic cells using quantitative image analysis. J. Cell Sci. 125, 5138–5150.

Smith, C.A., Lau, K.M., Rahmani, Z., Dho, S.E., Brothers, G., She, Y.M., Berry, D.M., Bonneil, E., Thibault, P., Schweisguth, F., et al. (2007). aPKC-mediated phosphorylation regulates asymmetric membrane localization of the cell fate determinant Numb. EMBO J. 26, 468–480.

Suzuki, A., and Ohno, S. (2006). The PAR-aPKC system: Lessons in polarity. J. Cell Sci. 119, 979–987.

Swaney, K.F., Huang, C.H., and Devreotes, P.N. (2010). Eukaryotic chemotaxis: A network of signaling pathways controls motility, directional sensing, and polarity. Annu. Rev. Biophys. 39, 265–289.

Tabuse, Y., Izumi, Y., Piano, F., Kemphues, K.J., Miwa, J., and Ohno, S. (1998). Atypical protein kinase C cooperates with PAR-3 to establish embryonic polarity in Caenorhabditis elegans. Development 125, 3607–3614.

Tian, A.G., and Deng, W.M. (2008). Lgl and its phosphorylation by aPKC regulate oocyte polarity formation in Drosophila. Development 135, 463–471.

Tostevin, F., and Howard, M. (2008). Modeling the establishment of PAR protein polarity in the one-cell C. elegans embryo. Biophys. J. 95, 4512–4522.

Weiner, O.D. (2002). Regulation of cell polarity during eukaryotic chemotaxis: The chemotactic compass. Curr. Opin. Cell Biol. 14, 196–202.

Zacharias, D.A., Violin, J.D., Newton, A.C., and Tsien, R.Y. (2002). Partitioning of lipid-modified monomeric GFPs into membrane microdomains of live cells. Science 296, 913–916.